Article

Study on Dynamic Snap-Through and Nonlinear Vibrations of an Energy Harvester Based on an Asymmetric Bistable Composite Laminated Shell

Ting Dong [1], Xinhua Chen [2,*] and Jun Zhang [2]

[1] Beijing Key Laboratory of Nonlinear Vibrations and Strength of Mechanical Structures, Faculty of Materials and Manufacturing, College of Mechanical Engineering and Applied Electronic Technology, Beijing University of Technology, Beijing 100124, China; dongting@emails.bjut.edu.cn

[2] Beijing Key Laboratory of Performance Guarantee on Urban Rail Transit Vehicles, Beijing University of Civil Engineering and Architecture, Beijing 102616, China; zhangjun611@bucea.edu.cn

* Correspondence: chenxinhua@bucea.edu.cn

Abstract: Bistable energy harvesters have been extensively studied. However, theoretical research on the dynamics of bistable energy harvesters based on asymmetric bistable composite laminated plate and shell structures has not been conducted. In this paper, a theoretical model on the dynamics of an energy harvester based on an asymmetric bistable composite laminated shell is established. The dynamic snap-through, the nonlinear vibrations and the voltage output with two potential wells of the bistable energy harvester are studied. The influence of the amplitude and the frequency for the base excitation on the bistable energy harvester is studied. When the frequency for the base excitation with a suitable amplitude in the frequency sweeping is located in a specific range or the amplitude for the base excitation with a suitable frequency in the amplitude sweeping is located in a specific range, the large-amplitude dynamic snap-through, nonlinear vibrations and voltage output with two potential wells can be found to occur. The amplitude and the frequency for the base excitation interact on each other for the specific amplitude or frequency range which migrates due to the softening nonlinearity. The vibration in the process of the dynamic snap-through behaves as the chaotic vibration. The nonlinear vibrations of the bistable system behave as the periodic vibration, the quasi-periodic vibration and the chaotic vibration. This study provides a theoretical reference for the design of energy harvesters based on asymmetric bistable composite laminated plate and shell structures.

Keywords: bistable energy harvesters; dynamic snap-through; nonlinear vibrations; chaotic vibration

1. Introduction

Bistable composite laminated plate and shell structures have two equilibrium configurations, so the large-amplitude dynamic snap-through and nonlinear vibrations may occur in dynamic environments, which greatly promotes the development of energy harvesters. The conventional energy harvesters integrated with bistable composite laminated plate and shell structures are designed as many kinds of bistable energy harvesters. Compared with conventional energy harvesters, bistable energy harvesters produce more strain and thus improve the power generation efficiency due to the large-amplitude dynamic snap-through and nonlinear vibrations with two potential wells. In fact, there have been several types of bistable energy harvesters based on different bistable structures. At present, the bistability of bistable energy harvesters can be realized by many ways. Specific boundary conditions and external forces can make structures buckle and thus obtain bistability [1–3]. In the manufacturing process, structures can realize bistability by applying the prestress to the materials [4–7]. When the plastic deformation or the inelastic deformation is applied to the materials, two or more stable equilibrium configurations can be obtained. The plastic deformation or the inelastic deformation is usually defined as Gaussian curvature effect [8–13].

The residual thermal stress formed in the curing process of asymmetric composite laminates can lead to two stable equilibrium configurations [14–21]. The integration of structures and bistable composite laminates can make the structures have two stable equilibrium configurations [22–24]. In this paper, an asymmetric bistable composite laminated shell for an energy harvester is adopted. The bistable shell is formed by an asymmetric composite laminated plate containing residual thermal stress which is naturally formed during curing. The greatest advantage of the asymmetric bistable composite laminated shell is that it is naturally formed by an asymmetric composite laminated plate through cooling from high temperature to room temperature without manual operations.

So far, some research on many different kinds of bistable energy harvesters has been carried out. Clamped–clamped buckled beams and cantilever beams for bistable energy harvesters were studied [25–27]. The magnetic forces were deployed to generate bistability [28,29]. Arrieta et al. [30] designed a nonlinear broadband energy harvester making use of a bistable plate and its nonlinearity. Lee and Inman [31] designed an asymmetric bistable composite laminated plate and shell structure by using two orthogonal MFCs (macro-fiber composites) for broadband energy harvesting. Syta et al. [32] utilized cross-well dynamics with snap-through of an asymmetric bistable composite laminated plate to enhance power generation capacity. Emam et al. [33] studied the snap-through and the period-doubling bifurcation of a bistable energy harvester based on an antisymmetric bistable composite laminated plate. Emam and Inman [34] summarized the developments and the principles of many different kinds of bistable energy harvesters. Pellegrini et al. [35] utilized the duffing oscillator to describe dynamics of all kinds of bistable energy harvesters. Lu et al. [36] performed research on energy harvesting during the passive vibration isolation. Single-well vibrations and the snap-through of bistable energy harvesters were also exhibited [37].

Above all, although there has been much research on many different kinds of bistable energy harvesters, the research on energy harvesters based on asymmetric bistable composite laminated plate and shell structures were focused on experiments. As the asymmetric bistable composite laminated plate and shell structures are naturally formed by asymmetric composite laminates through cooling from high temperature to room temperature without manual operations, it is very necessary and meaningful to study energy harvesters based on asymmetric bistable composite laminated plate and shell structures theoretically.

In this paper, a dynamic model of an energy harvester based on an asymmetric bistable composite laminated shell is established. The influence of the base excitation amplitude and frequency on the bistable energy harvester is studied. The frequency sweeping with a constant amplitude and the amplitude sweeping with a constant frequency are carried out respectively. The dynamic snap-through, the nonlinear vibrations and the voltage output with two potential wells of the bistable energy harvester are given. When the frequency for the base excitation with a suitable amplitude is located in a specific range in the frequency sweeping or the amplitude for the base excitation with a suitable frequency is located in a specific range in the amplitude sweeping, the large-amplitude dynamic snap-through, nonlinear vibrations and voltage output with two potential wells can be found to occur. That is to say, deploying only one parameter amplitude or frequency for the base excitation cannot maximize the optimization of the bistable energy harvester. When the amplitude and the frequency for the base excitation jointly achieve the maximum optimization, the large-amplitude dynamic snap-through and voltage output can be realized in a very ideal amplitude or frequency range for the base excitation.

2. Dynamic Model

In order to determine the two stable equilibrium configurations formed after curing of the asymmetric composite laminated plate shown in Figure 1, the displacement field can be written based on the classical plate theory in Ref. [38] as follows

$$u(x,y,z,t) = u_0(x,y,t) - z\frac{\partial w}{\partial x}, \tag{1}$$

$$v(x,y,z,t) = v_0(x,y,t) - z\frac{\partial w}{\partial y}, \qquad (2)$$

$$w(x,y,t) = w_0(x,y,t). \qquad (3)$$
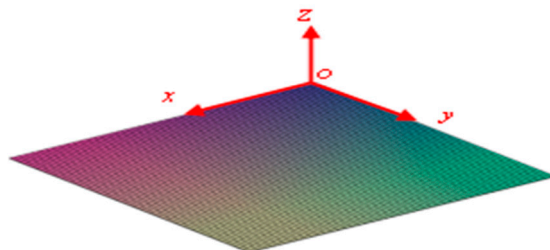
Figure 1. The asymmetric composite laminated plate $[0/0/0/0/90/90/90/90]$ before curing.

Based on the von Kármán's large deformation theory in Ref. [38], the nonlinear strain-displacement relationship can be determined:

$$\left\{\begin{array}{c} \varepsilon_x \\ \varepsilon_y \\ \gamma_{xy} \end{array}\right\} = \left\{\begin{array}{c} \varepsilon_x^{(0)} \\ \varepsilon_y^{(0)} \\ \gamma_{xy}^{(0)} \end{array}\right\} + z\left\{\begin{array}{c} \varepsilon_{xx}^{(1)} \\ \varepsilon_{yy}^{(1)} \\ \gamma_{xy}^{(1)} \end{array}\right\}, \qquad (4)$$

$$\left\{\begin{array}{c} \varepsilon_{xx}^{(0)} \\ \varepsilon_{yy}^{(0)} \\ \gamma_{xy}^{(0)} \end{array}\right\} = \left\{\begin{array}{c} \frac{\partial u_0}{\partial x} + \frac{1}{2}\left(\frac{\partial w_0}{\partial x}\right)^2 \\ \frac{\partial v_0}{\partial y} + \frac{1}{2}\left(\frac{\partial w_0}{\partial y}\right)^2 \\ \frac{\partial u_0}{\partial y} + \frac{\partial v_0}{\partial x} + \frac{\partial w_0}{\partial x}\frac{\partial w_0}{\partial y} \end{array}\right\}, \quad \left\{\begin{array}{c} \varepsilon_{xx}^{(1)} \\ \varepsilon_{yy}^{(1)} \\ \gamma_{xy}^{(1)} \end{array}\right\} = \left\{\begin{array}{c} -\frac{\partial^2 w_0}{\partial x^2} \\ -\frac{\partial^2 w_0}{\partial y^2} \\ -2\frac{\partial^2 w_0}{\partial x \partial y} \end{array}\right\}. \qquad (5)$$

The constitutive relation of the asymmetric composite laminated plate is

$$\left\{\begin{array}{c} \sigma_x \\ \sigma_y \\ \sigma_{xy} \end{array}\right\} = \left[\begin{array}{ccc} \overline{Q}_{11} & \overline{Q}_{12} & \overline{Q}_{16} \\ \overline{Q}_{12} & \overline{Q}_{22} & \overline{Q}_{26} \\ \overline{Q}_{16} & \overline{Q}_{26} & \overline{Q}_{66} \end{array}\right]\left\{\left\{\begin{array}{c} \varepsilon_x \\ \varepsilon_y \\ \varepsilon_{xy} \end{array}\right\} - \left\{\begin{array}{c} \overline{\alpha}_{xx} \\ \overline{\alpha}_{yy} \\ \overline{\alpha}_{xy} \end{array}\right\}\Delta T\right\}, \qquad (6)$$

where ΔT denotes the difference between the room temperature and the manufacturing temperature, and

$$\begin{aligned} \overline{Q}_{11} &= Q_{11}\cos^4\theta + 2(Q_{12} + 2Q_{66})\sin^2\theta\cos^2\theta + Q_{22}\sin^4\theta, \\ \overline{Q}_{12} &= (Q_{11} + Q_{22} - 4Q_{66})\sin^2\theta\cos^2\theta + Q_{12}\left(\sin^4\theta + \cos^4\theta\right), \\ \overline{Q}_{22} &= Q_{11}\sin^4\theta + 2(Q_{12} + 2Q_{66})\sin^2\theta\cos^2\theta + Q_{22}\cos^4\theta, \\ \overline{Q}_{16} &= (Q_{11} - Q_{12} - 2Q_{66})\sin\theta\cos^3\theta + (Q_{12} - Q_{22} + 2Q_{66})\sin^3\theta\cos\theta, \\ \overline{Q}_{26} &= (Q_{11} - Q_{12} - 2Q_{66})\sin^3\theta\cos\theta + (Q_{12} - Q_{22} + 2Q_{66})\sin\theta\cos^3\theta, \\ \overline{Q}_{66} &= (Q_{11} + Q_{22} - 2Q_{12} - 2Q_{66})\sin^2\theta\cos^2\theta + Q_{66}\left(\sin^4\theta + \cos^4\theta\right), \\ \overline{\alpha}_{xx} &= \alpha_{xx}\cos^2\theta + \alpha_{yy}\sin^2\theta, \quad \overline{\alpha}_{yy} = \alpha_{xx}\sin^2\theta + \alpha_{yy}\cos^2\theta, \\ \overline{\alpha}_{xy} &= (\alpha_{xx} - \alpha_{yy})\sin\theta\cos\theta, \end{aligned} \qquad (7)$$

where

$$\begin{aligned} Q_{11} &= \frac{E_{11}}{1 - v_{12}v_{21}}, \ Q_{22} = \frac{E_{22}}{1 - v_{12}v_{21}}, \ Q_{12} = \frac{E_{22}v_{12}}{1 - v_{12}v_{21}}, \ Q_{16} = Q_{26} = 0, \\ Q_{45} &= 0, \ Q_{44} = Q_{55} = G_{13}, \ Q_{66} = G_{12} \end{aligned} \qquad (8)$$

Based on Equations (1)–(8), the potential energy of the asymmetric composite laminated plate can be determined

$$U_{\text{Lam}1} = \frac{1}{2}\int_{V_{\text{Lam}}} (\sigma_{xx}\varepsilon_{xx} + \sigma_{yy}\varepsilon_{yy} + \sigma_{xy}\gamma_{xy})dV_{\text{Lam}}, \qquad (9)$$

where the V_{Lam} denotes the volume of the asymmetric composite laminated plate.

In order to determine the static equilibrium configurations, u_0, v_0 and w_0 in Equations (1)–(5) are replaced by static displacements u_s^{I}, v_s^{I} and w_s^{I}.

According to Refs. [38,39], the static displacement field can be set as

$$u_s^{\text{I}} = \sum_{m=0}^{M} \sum_{n=0}^{m} u_{n,m-n} x^n y^{m-n}, \tag{10}$$

$$v_s^{\text{I}} = \sum_{m=0}^{M} \sum_{n=0}^{m} v_{n,m-n} x^n y^{m-n}, \tag{11}$$

$$w_s^{\text{I}} = \sum_{m=0}^{M} \sum_{n=0}^{m} w_{n,m-n} x^n y^{m-n}. \tag{12}$$

The principle of minimum potential energy can be expressed in the following form

$$f_i = \frac{\partial U_{\text{Lam1}}}{\partial X_i}, \ (i = 1, 2, 3), \tag{13}$$

where the U_{Lam1} denotes the potential energy of the asymmetric composite laminated plate, and $X_1 = u_s^{\text{I}}$, $X_2 = v_s^{\text{I}}$ and $X_3 = w_s^{\text{I}}$.

Setting the absolute value of the temperature difference $|\Delta T|$ as the control parameter and solving f_1, f_2 and f_3 by Equations (9)–(13), the static bifurcation diagram Figure 2 can be graphically presented as below.
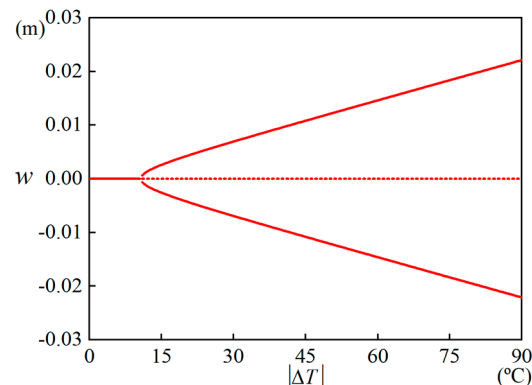
Figure 2. The static bifurcation diagram for the asymmetric composite laminated plate.

When ΔT is set to $-90\,^{\circ}\text{C}$, the asymmetric composite laminated plate generates two stable equilibrium states with large deformation. However, when ΔT is too small, the deformation is not obvious, and when ΔT is too large, the manufacturing cost is increased.

Making $\Delta T = -90\,^{\circ}\text{C}$, u_{s1}^{I}, v_{s1}^{I} and w_{s1}^{I} corresponding to the lower stable equilibrium configuration and u_{s2}^{I}, v_{s2}^{I} and w_{s2}^{I} corresponding to the upper stable equilibrium configuration can be determined shown in Figure 3.

Compared to a simple piezoelectric layer, the energy approach based on the MFC is similar. Since the two stable states of the bistable structure behave as cylindrical shells, the simple piezoelectric layer may significantly reduce the curvature and weaken the bistability of the bistable structure, while the MFC can guarantee the bistability of the bistable structure. Moreover, the MFC can be used to actuate the snap-through, which will be introduced in the next stage.

Since the MFC is to be attached to the surface of the shell, the plate model above must be transformed into a shell model.

Due to the stiffness of the MFC itself, new deformations can occur in the process of attaching the MFC to the surface of the bistable shell, which produces new equilibrium positions.
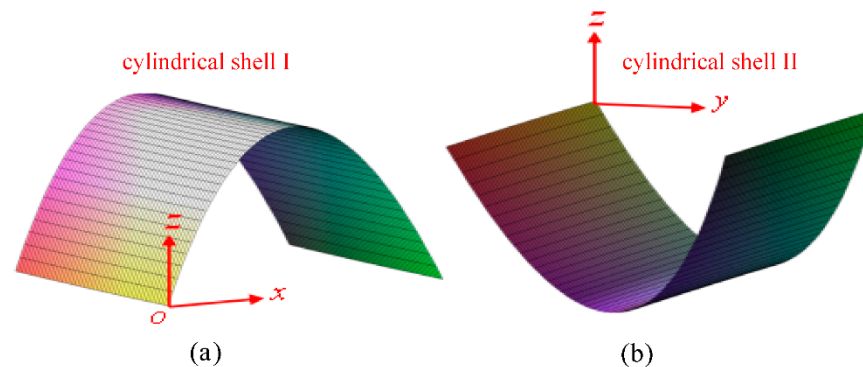
Figure 3. The two stable cylindrical shells after curing, (**a**) the cylindrical Shell I, (**b**) the cylindrical Shell II.

Setting u_{s1}^{I}, v_{s1}^{I} and w_{s1}^{I} as initial equilibrium positions and combining with Equations (1)–(3), the displacement field of the bistable shell can be obtained:

$$u(x,y,z,t) = u_0(x,y,t) + u_{s1}^{\mathrm{I}} - z\frac{\partial\left(w_0 + w_{s1}^{\mathrm{I}}\right)}{\partial x}, \tag{14}$$

$$v(x,y,z,t) = v_0(x,y,t) + v_{s1}^{\mathrm{I}} - z\frac{\partial\left(w_0 + w_{s1}^{\mathrm{I}}\right)}{\partial y}, \tag{15}$$

$$w(x,y,t) = w_0(x,y,t) + w_{s1}^{\mathrm{I}}. \tag{16}$$

The new nonlinear strain-displacement relationship can be determined

$$\left\{\begin{array}{c}\varepsilon_x \\ \varepsilon_y \\ \gamma_{xy}\end{array}\right\} = \left\{\begin{array}{c}\varepsilon_x^{(0)} \\ \varepsilon_y^{(0)} \\ \gamma_{xy}^{(0)}\end{array}\right\} + z\left\{\begin{array}{c}\varepsilon_{xx}^{(1)} \\ \varepsilon_{yy}^{(1)} \\ \gamma_{xy}^{(1)}\end{array}\right\}, \tag{17}$$

$$\left\{\begin{array}{c}\varepsilon_{xx}^{(0)} \\ \varepsilon_{yy}^{(0)} \\ \gamma_{xy}^{(0)}\end{array}\right\} = \left\{\begin{array}{c}\dfrac{\partial\left(u_0 + u_{s1}^{\mathrm{I}}\right)}{\partial x} + \dfrac{1}{2}\left(\dfrac{\partial\left(w_0 + w_{s1}^{\mathrm{I}}\right)}{\partial x}\right)^2 \\ \dfrac{\partial\left(v_0 + v_{s1}^{\mathrm{I}}\right)}{\partial y} + \dfrac{1}{2}\left(\dfrac{\partial\left(w_0 + w_{s1}^{\mathrm{I}}\right)}{\partial y}\right)^2 \\ \dfrac{\partial\left(u_0 + u_{s1}^{\mathrm{I}}\right)}{\partial y} + \dfrac{\partial\left(v_0 + v_{s1}^{\mathrm{I}}\right)}{\partial x} + \left(\dfrac{\partial\left(w_0 + w_{s1}^{\mathrm{I}}\right)}{\partial x}\right)\left(\dfrac{\partial\left(w_0 + w_{s1}^{\mathrm{I}}\right)}{\partial y}\right)\end{array}\right\}, \tag{18}$$

$$\left\{\begin{array}{c}\varepsilon_{xx}^{(1)} \\ \varepsilon_{yy}^{(1)} \\ \gamma_{xy}^{(1)}\end{array}\right\} = \left\{\begin{array}{c}-\dfrac{\partial^2\left(w_0 + w_{s1}^{\mathrm{I}}\right)}{\partial x^2} \\ -\dfrac{\partial^2\left(w_0 + w_{s1}^{\mathrm{I}}\right)}{\partial y^2} \\ -2\dfrac{\partial^2\left(w_0 + w_{s1}^{\mathrm{I}}\right)}{\partial x \partial y}\end{array}\right\}. \tag{19}$$

To determine the new equilibrium positions, the potential energy must be recalculated, and the principle of minimum potential energy must be carried out again.

The constitutive relationship for the shell of the MFC–bistable composite laminated shell structure is

$$\left\{\begin{array}{c}\sigma_x \\ \sigma_y \\ \sigma_{xy}\end{array}\right\} = \left[\begin{array}{ccc}\overline{Q}_{11} & \overline{Q}_{12} & \overline{Q}_{16} \\ \overline{Q}_{12} & \overline{Q}_{22} & \overline{Q}_{26} \\ \overline{Q}_{16} & \overline{Q}_{26} & \overline{Q}_{66}\end{array}\right]\left\{\left\{\begin{array}{c}\varepsilon_x \\ \varepsilon_y \\ \varepsilon_{xy}\end{array}\right\} - \left\{\begin{array}{c}\overline{\alpha}_{xx} \\ \overline{\alpha}_{yy} \\ \overline{\alpha}_{xy}\end{array}\right\}\Delta T\right\}, \tag{20}$$

where ΔT denotes the difference between the room temperature and the manufacturing temperature, and

$$
\begin{aligned}
\overline{Q}_{11} &= Q_{11}\cos^4\theta + 2(Q_{12} + 2Q_{66})\sin^2\theta\cos^2\theta + Q_{22}\sin^4\theta, \\
\overline{Q}_{12} &= (Q_{11} + Q_{22} - 4Q_{66})\sin^2\theta\cos^2\theta + Q_{12}\left(\sin^4\theta + \cos^4\theta\right), \\
\overline{Q}_{22} &= Q_{11}\sin^4\theta + 2(Q_{12} + 2Q_{66})\sin^2\theta\cos^2\theta + Q_{22}\cos^4\theta, \\
\overline{Q}_{16} &= (Q_{11} - Q_{12} - 2Q_{66})\sin\theta\cos^3\theta + (Q_{12} - Q_{22} + 2Q_{66})\sin^3\theta\cos\theta, \\
\overline{Q}_{26} &= (Q_{11} - Q_{12} - 2Q_{66})\sin^3\theta\cos\theta + (Q_{12} - Q_{22} + 2Q_{66})\sin\theta\cos^3\theta, \\
\overline{Q}_{66} &= (Q_{11} + Q_{22} - 2Q_{12} - 2Q_{66})\sin^2\theta\cos^2\theta + Q_{66}\left(\sin^4\theta + \cos^4\theta\right), \\
\overline{\alpha}_{xx} &= \alpha_{xx}\cos^2\theta + \alpha_{yy}\sin^2\theta, \; \overline{\alpha}_{yy} = \alpha_{xx}\sin^2\theta + \alpha_{yy}\cos^2\theta, \\
\overline{\alpha}_{xy} &= \left(\alpha_{xx} - \alpha_{yy}\right)\sin\theta\cos\theta,
\end{aligned}
\tag{21}
$$

where

$$
Q_{11} = \frac{E_{11}}{1 - v_{12}v_{21}}, \; Q_{22} = \frac{E_{22}}{1 - v_{12}v_{21}}, \; Q_{12} = \frac{E_{22}v_{12}}{1 - v_{12}v_{21}}, \; Q_{16} = Q_{26} = 0,
$$
$$
Q_{45} = 0, \; Q_{44} = Q_{55} = G_{13}, \; Q_{66} = G_{12}.
\tag{22}
$$

Equations (6), (7), (20) and (21) are the same in form but different in content. Equations (6) and (7) denote the plate, while Equations (20) and (21) denote the shell.

The constitutive relationship for the MFC of the MFC–bistable composite laminated shell structure is

$$
\left\{
\begin{array}{c}
\sigma_{xx}^E \\
\sigma_{yy}^E \\
\sigma_{xy}^E \\
D_z
\end{array}
\right\}
=
\left[
\begin{array}{cccc}
c_{11}^E & c_{12}^E & 0 & -e_{31} \\
c_{12}^E & c_{22}^E & 0 & -e_{32} \\
0 & 0 & c_{66}^E & 0 \\
e_{31} & e_{32} & 0 & \varepsilon_{33}^s
\end{array}
\right]
\left\{
\begin{array}{c}
\varepsilon_x \\
\varepsilon_y \\
\varepsilon_{xy} \\
E_z
\end{array}
\right\}.
\tag{23}
$$

Based on Equations (14)–(22), the potential energy of the bistable shell in the structure is recalculated as

$$
U_{\text{Lam2}} = \frac{1}{2}\int_{V_{\text{Lam}}} \left(\sigma_{xx}\varepsilon_{xx} + \sigma_{yy}\varepsilon_{yy} + \sigma_{xy}\gamma_{xy}\right)dV_{\text{Lam}}.
\tag{24}
$$

Based on Equations (14)–(19) and (23), the potential energy of the MFC in the structure is

$$
\left(U_{\text{pie}}\right)_{\text{m}} = \frac{1}{2}\int_{V_{\text{pie}}} \left(\sigma_{xx}^E\varepsilon_{xx}^E + \sigma_{yy}^E\varepsilon_{yy}^E + \sigma_{xy}^E\gamma_{xy}^E\right)dV_{\text{pie}}.
\tag{25}
$$

The total potential energy of the MFC–bistable composite laminated shell structure is

$$
U_{\text{total}} = U_{\text{Lam2}} + \left(U_{\text{pie}}\right)_{\text{m}}.
\tag{26}
$$

The principle of minimum potential energy is re-expressed as follows

$$
\delta U_{\text{total}} = \sum_{i=1}^{3} \frac{\partial U_{\text{total}}}{\partial Y_i}\delta Y_i, \; (i = 1, 2, 3).
\tag{27}
$$

By solving Equation (27), the deformations Δu_{s1}^{I}, Δv_{s1}^{I} and Δw_{s1}^{I} in the process of attaching the MFC to the surface of the bistable shell can be determined.

The new equilibrium positions can be expressed

$$
u_s^{\text{II}} = u_{s1}^{\text{I}} + \Delta u_{s1}^{\text{I}},
\tag{28}
$$

$$
v_s^{\text{II}} = v_{s1}^{\text{I}} + \Delta v_{s1}^{\text{I}},
\tag{29}
$$

$$
w_s^{\text{II}} = w_{s1}^{\text{I}} + \Delta w_{s1}^{\text{I}}.
\tag{30}
$$

Finally, the energy harvester based on the asymmetric bistable composite laminated shell is determined shown in Figure 4.

new cylindrical shell I

new cylindrical shell II

(a)

(b)
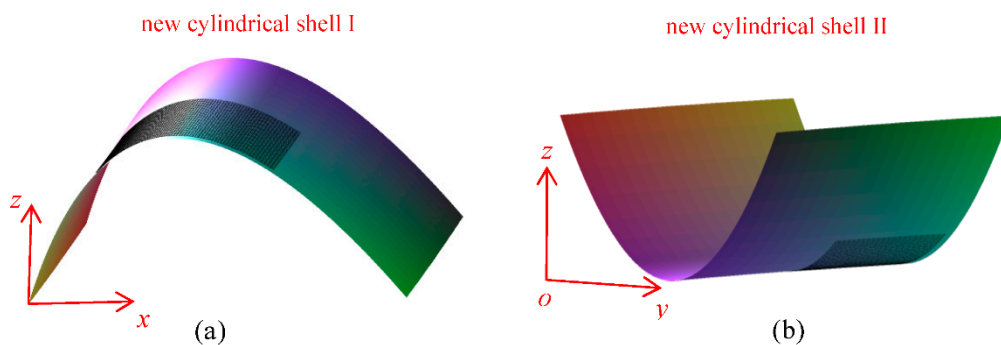
Figure 4. The two new stable cylindrical shells with a piezoelectric patch on the surface, (**a**) the cylindrical Shell I, (**b**) the cylindrical Shell II.

In order to establish the dynamic model shown in Figure 5 for the bistable energy harvester, the displacement field must be written as follows

$$u(x,y,z,t) = u_0(x,y,t) + u_s^{\text{II}} - z\frac{\partial\left(w_0 + w_s^{\text{II}}\right)}{\partial x}, \tag{31}$$

$$v(x,y,z,t) = v_0(x,y,t) + v_s^{\text{II}} - z\frac{\partial\left(w_0 + w_s^{\text{II}}\right)}{\partial y}, \tag{32}$$

$$w(x,y,t) = w_0(x,y,t) + w_s^{\text{II}} + Y, \tag{33}$$

where Y is the base excitation.

R

MFC

the bistable shell

$Y = Y(t)$
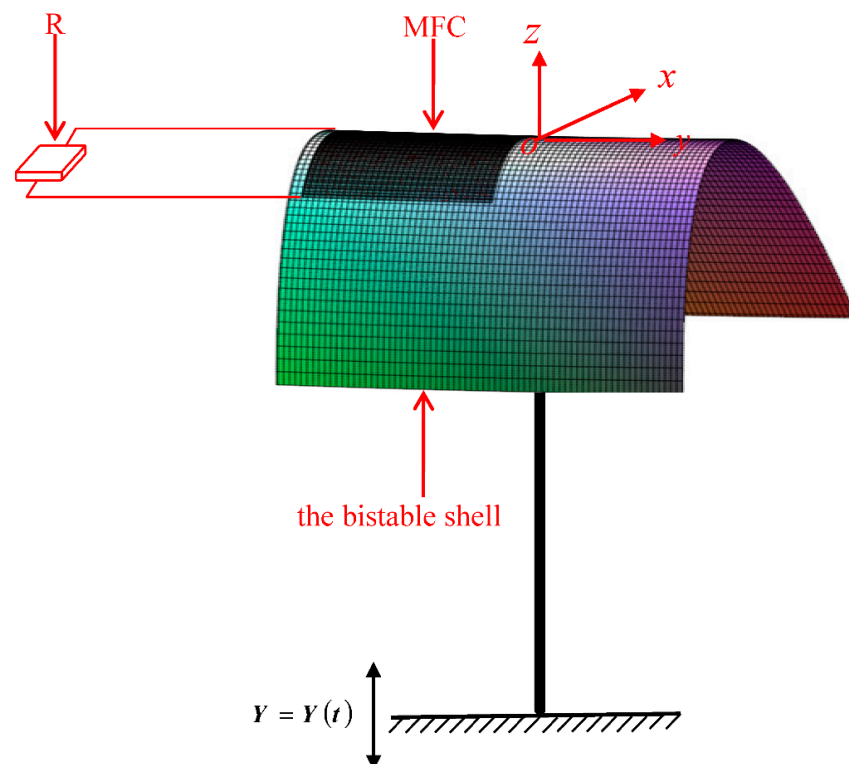
Figure 5. The dynamic model for the bistable energy harvester based on the asymmetric bistable composite laminated shell.

The nonlinear strain-displacement relationship of the MFC–bistable shell structure is rewritten as

$$
\left\{ \begin{array}{c} \varepsilon_x \\ \varepsilon_y \\ \gamma_{xy} \end{array} \right\} = \left\{ \begin{array}{c} \varepsilon_x^{(0)} \\ \varepsilon_y^{(0)} \\ \gamma_{xy}^{(0)} \end{array} \right\} + z \left\{ \begin{array}{c} \varepsilon_{xx}^{(1)} \\ \varepsilon_{yy}^{(1)} \\ \gamma_{xy}^{(1)} \end{array} \right\}
\tag{34}
$$

$$
\left\{ \begin{array}{c} \varepsilon_{xx}^{(0)} \\ \varepsilon_{yy}^{(0)} \\ \gamma_{xy}^{(0)} \end{array} \right\} = \left\{ \begin{array}{c} \dfrac{\partial\left(u_0+u_s^{\mathrm{II}}\right)}{\partial x} + \dfrac{1}{2}\left(\dfrac{\partial\left(w_0+w_s^{\mathrm{II}}\right)}{\partial x}\right)^2 \\[2mm] \dfrac{\partial\left(v_0+v_s^{\mathrm{II}}\right)}{\partial y} + \dfrac{1}{2}\left(\dfrac{\partial\left(w_0+w_s^{\mathrm{II}}\right)}{\partial y}\right)^2 \\[2mm] \dfrac{\partial\left(u_0+u_s^{\mathrm{II}}\right)}{\partial y} + \dfrac{\partial\left(v_0+v_s^{\mathrm{II}}\right)}{\partial x} + \left(\dfrac{\partial\left(w_0+w_s^{\mathrm{II}}\right)}{\partial x}\right)\left(\dfrac{\partial\left(w_0+w_s^{\mathrm{II}}\right)}{\partial y}\right) \end{array} \right\}
\tag{35}
$$

$$
\left\{ \begin{array}{c} \varepsilon_{xx}^{(1)} \\ \varepsilon_{yy}^{(1)} \\ \gamma_{xy}^{(1)} \end{array} \right\} = \left\{ \begin{array}{c} -\dfrac{\partial^2\left(w_0+w_s^{\mathrm{II}}\right)}{\partial x^2} \\[2mm] -\dfrac{\partial^2\left(w_0+w_s^{\mathrm{II}}\right)}{\partial y^2} \\[2mm] -2\dfrac{\partial^2\left(w_0+w_s^{\mathrm{II}}\right)}{\partial x\partial y} \end{array} \right\}
\tag{36}
$$

Based on Equations (20)–(22) and (28)–(36), the potential energy of the bistable shell in the structure is redefined as

$$
U_{\mathrm{Lam3}} = \frac{1}{2}\int_{V_{\mathrm{Lam}}} \left(\sigma_{xx}\varepsilon_{xx} + \sigma_{yy}\varepsilon_{yy} + \sigma_{xy}\gamma_{xy}\right)dV_{\mathrm{Lam}}.
\tag{37}
$$

Based on Equations (23) and (28)–(36), the potential energy of the MFC in the structure is the sum of its own strain energy and the electric potential energy after energization.

$$
U_{\mathrm{pie}} = \frac{1}{2}\int_{V_{\mathrm{pie}}} \left(\sigma_{xx}^E\varepsilon_{xx}^E + \sigma_{yy}^E\varepsilon_{yy}^E + \sigma_{xy}^E\varepsilon_{xy}^E\right)dV_{\mathrm{pie}} - \int_{V_{\mathrm{pie}}} \left(E_z e_{31}\varepsilon_{xx}^E + E_z e_{32}\varepsilon_{yy}^E\right)dV_{\mathrm{pie}}.
\tag{38}
$$

The kinetic energy of the bistable shell in the structure is defined as

$$
T_{\mathrm{Lam}} = \frac{1}{2}\rho_{\mathrm{Lam}}\int_{V_{\mathrm{Lam}}} \left(\dot{u}^2 + \dot{v}^2 + \dot{w}^2\right)dV_{\mathrm{Lam}}
\tag{39}
$$

The kinetic energy of the MFC in the structure is defined as

$$
T_{\mathrm{pie}} = \frac{1}{2}\rho_{\mathrm{pie}}\int_{V_{\mathrm{pie}}} \left(\dot{u}^2 + \dot{v}^2 + \dot{w}^2\right)dV_{\mathrm{pie}}
\tag{40}
$$

The work performed by the electric field in the direction of potential shift is

$$
W_{ie} = \frac{1}{2}\int_{V_{\mathrm{pie}}} \left(E_z D_z\right)dV_{\mathrm{pie}}
\tag{41}
$$

The potential shift D_z is homogenized in the thickness direction

$$
\widetilde{D}_z = \frac{\int_H^{H+h_p}\left(e_{31}\varepsilon_x + e_{32}\varepsilon_y + \varepsilon_{33}^s E_z\right)}{h_p}
\tag{42}
$$

The electric charge quantity is calculated

$$
Q(t) = -\iint_{\Omega_{\mathrm{pie}}} \widetilde{D}_z dx dy
\tag{43}
$$

An energy balance is introduced

$$\int V(t)I(t)dt = V(t)Q(t), \tag{44}$$

where $V(t)$ is the voltage and $Q(t)$ is the electric quantity.

The work performed by external forces is

$$W = \int_{V_{\text{total}}} (-c\dot{w}w)dV_{\text{total}} - V(t)Q(t), \tag{45}$$

where c is the damping coefficient.

The relationship between the current and the voltage is as follows

$$V(t) = I(t)R = -R\dot{Q}(t), \tag{46}$$

where R is the external electrical resistance, and $I(t)$ is the current.

The Hamilton's principle according to Ref. [38] is given as

$$\delta \int_{t_1}^{t_2} L = 0, \tag{47}$$

where

$$L = T_{\text{Lam}} + T_{\text{pie}} - U_{\text{Lam3}} - U_{\text{pie}} + W_{ie} + W. \tag{48}$$

In order to study the dynamic snap-through, the nonlinear vibrations and the voltage output with two potential wells of the bistable energy harvester, the dynamic displacements according to Ref. [39] are set as

$$u_0(x,y,t) = \sum_{m=0}^{N}\sum_{n=0}^{m} u_{n,m-n}(t)x^n y^{n-m}, \tag{49}$$

$$v_0(x,y,t) = \sum_{m=0}^{N}\sum_{n=0}^{m} v_{n,m-n}(t)x^n y^{n-m}, \tag{50}$$

$$w_0(x,y,t) = \sum_{m=0}^{N}\sum_{n=0}^{m} w_{n,m-n}(t)x^n y^{n-m}. \tag{51}$$

Substituting Equations (37)–(46) and (49)–(51) into Equation (47), integrating on plane ($x\in[-L_x, L_x]$ and $y\in[-L_y, L_y]$), selecting the first three degrees of freedom and introducing dimensionless parameters,

$$\begin{aligned}
&\bar{u}_1 = u_1,\ \bar{u}_2 = L_y^2 u_2,\ \bar{u}_3 = L_x^2 u_3,\ \bar{v}_1 = v_1,\ \bar{v}_2 = L_x^2 v_2,\ \bar{v}_3 = L_y^2 v_3,\\
&\bar{w}_1 = L_x w_1,\ \bar{w}_2 = L_y w_2
\end{aligned} \tag{52}$$

dimensionless ordinary differential equations can be obtained

$$\begin{aligned}
&\ddot{\bar{w}}_1 + \bar{c}_1\dot{\bar{w}}_1 + \bar{k}_1\bar{w}_1 + \bar{k}_2\bar{w}_2 + \overline{N}_1\bar{w}_1 + \overline{N}_2\bar{w}_2 + \overline{N}_3 + \overline{V}_1\bar{w}_1 + \overline{V}_2\bar{w}_2 + \overline{V}_3 + \bar{a}_{11}\bar{w}_1^2 + \bar{a}_{12}\bar{w}_2^2\\
&+\bar{a}_{13}\bar{w}_1\bar{w}_2 + \bar{a}_{14}\bar{w}_1^3 + \bar{a}_{15}\bar{w}_2^3 + \bar{a}_{16}\bar{w}_1^2\bar{w}_2 + \bar{a}_{17}\bar{w}_1\bar{w}_2^2 = \bar{f}\cos(\overline{\Omega}t),
\end{aligned} \tag{53}$$

$$\begin{aligned}
&\ddot{\bar{w}}_2 + \bar{c}_2\dot{\bar{w}}_2 + \bar{k}_3\bar{w}_1 + \bar{k}_4\bar{w}_2 + \overline{N}_4\bar{w}_1 + \overline{N}_5\bar{w}_2 + \overline{N}_6 + \overline{V}_4\bar{w}_1 + \overline{V}_5\bar{w}_2 + \overline{V}_6 + \bar{a}_{21}\bar{w}_1^2 + \bar{a}_{22}\bar{w}_2^2\\
&+\bar{a}_{23}\bar{w}_1\bar{w}_2 + \bar{a}_{24}\bar{w}_1^3 + \bar{a}_{25}\bar{w}_2^3 + \bar{a}_{26}\bar{w}_1^2\bar{w}_2 + \bar{a}_{27}\bar{w}_1\bar{w}_2^2 = \bar{f}\cos(\overline{\Omega}t),
\end{aligned} \tag{54}$$

$$\dot{\overline{V}} + \bar{a}_{31}\overline{V} + \bar{a}_{32}\bar{w}_1\dot{\bar{w}}_1 + \bar{a}_{33}\bar{w}_2\dot{\bar{w}}_1 + \bar{a}_{34}\dot{\bar{w}}_1 + \bar{a}_{35}\bar{w}_1\dot{\bar{w}}_2 + \bar{a}_{36}\bar{w}_2\dot{\bar{w}}_2 + \bar{a}_{37}\dot{\bar{w}}_2 = 0 \tag{55}$$

The coefficients in Equations (53)–(55) can be determined by material properties shown in Tables 1 and 2 and step-by-step numerical calculations from Equation (1) to Equation (55). Based on Ref. [40], the Tables 1 and 2 take the following form.

Table 1. Material properties of the bistable asymmetric composite laminated shell.

Properties	Description	Data	Unit
E_{11}	The longitudinal modulus	147	GPa
E_{22}	The transverse modulus	10.7	GPa
G_{12}	The shear modulus	7	GPa
G_{13}	The shear modulus	7	GPa
G_{23}	The shear modulus	7	GPa
ν_{12}	The major Poisson's ratio	0.3	–
α_1	The longitudinal coefficient of thermal expansion	5×10^{-7}	$[^\circ\text{C}]^{-1}$
α_2	The transversal coefficient of thermal expansion	2.649×10^{-5}	$[^\circ\text{C}]^{-1}$
h	The thickness of the fiber	0.122	mm
L_x	The length of the fiber	300	mm
L_y	The width of the fiber	300	mm

Table 2. Material properties of the MFC.

Properties	Description	Data	Unit
E_{11}	The longitudinal modulus	30.336	GPa
E_{22}	The transverse modulus	15.857	GPa
G_{12}	The shear modulus	5.515	GPa
G_{13}	The shear modulus	5.515	GPa
G_{23}	The shear modulus	6.823	GPa
ν_{12}	The major Poisson's ratio	0.31	–
e_{31} [10^{-9} mm/V]	The piezoelectric constant	-210	10^{-9} mm/V
e_{32} [10^{-9} mm/V]	The piezoelectric constant	-210	10^{-9} mm/V
e_{33} [10^{-9} mm/V]	The piezoelectric constant	460	10^{-9} mm/V
h	The thickness of the MFC	0.3	mm
L_x	The length of the MFC	85	mm
L_y	The width of the MFC	57	mm

The physical parameters in Table 1 are measured directly in the laboratory. The physical parameters in Table 2 are determined according to Ref. [41].

3. Numerical Simulation

In order to study the dynamic snap-through, the nonlinear vibrations and the voltage output with two potential wells of the energy harvester based on the asymmetric bistable composite laminated shell, the Runge–Kutta method is adopted to solve Equations (53)–(55). The bifurcation diagram, the time-history graph, the Poincaré map, the amplitude-frequency curve and the spectrum diagram are demonstrated. Dimensionless symbols are omitted in Equations (53)–(55) for convenience. The influence of the base excitation amplitude f and frequency Ω on the bistable energy harvester is studied.

3.1. Dynamic Snap-Through and Nonlinear Vibrations

The time-history diagrams, the spectrum diagrams and the Poincaré maps are graphically presented in Figures 6–11, which represent different vibrations based on different operating conditions. When the insufficient energy is applied, the vibration of the system revolves around either the upper stable state or the lower stable state shown in Figure 6, while when the sufficient energy is applied, the system vibrates between the two stable states, which denotes the dynamic snap-through shown in Figures 7 and 11. The dynamic snap-through is elaborated in Figures 7 and 11 delivering the vibrations around the

two stable states respectively and the dynamic snap-through between the two stable states. The vibration in the process of the dynamic snap-through behaves as the chaotic vibration which is the nonlinear vibration with two potential wells due to the two stable equilibrium positions. The nonlinear vibrations of the bistable system in the whole process behave as the periodic vibration, the quasi-periodic vibration and the chaotic vibration based on the Poincaré maps shown in Figures 9–11. Similarly, the vibrations of the bistable system can be detected by the spectrum diagrams. The vibration of the system revolves around either the upper stable state or the lower stable state behaves as the periodic vibration or the quasi-periodic vibration according to the spectrum diagrams in Figure 6b,c, where the response of the system is excited only at a certain frequency. Based on the spectrum diagram in Figure 7b, where the responses of the system are excited in a broadband, the vibration in the process of the dynamic snap-through behaves as the chaotic vibration.
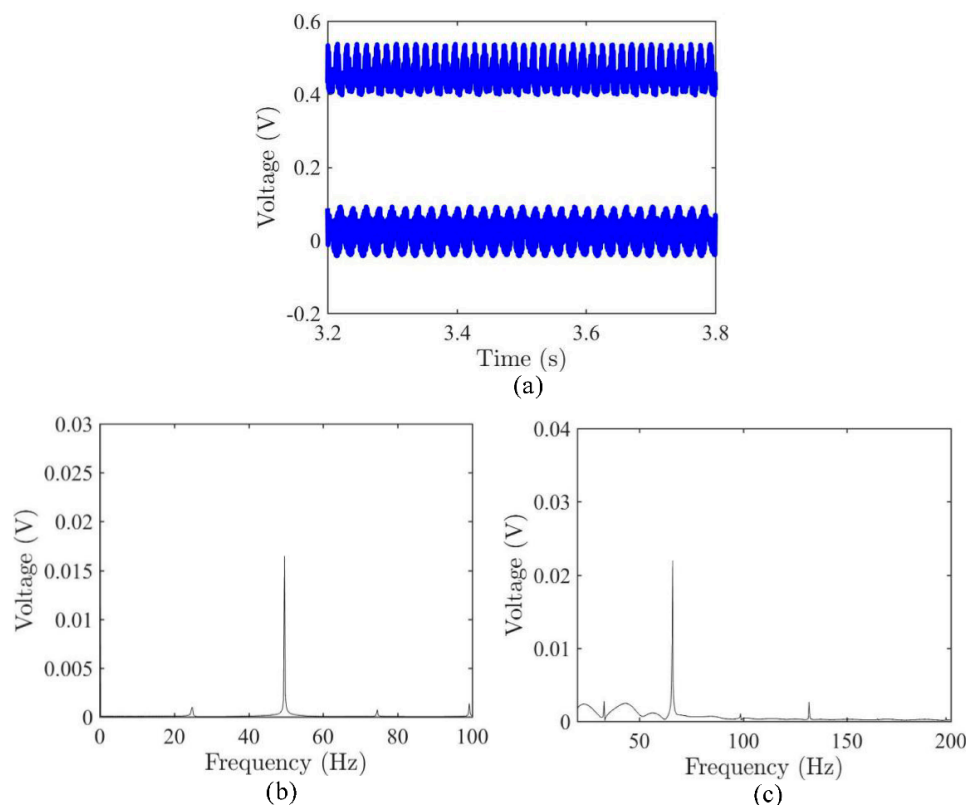
Figure 6. The voltage outputs around the two stable states respectively, (**a**) the time-history graphs around the two stable states respectively, (**b**) the spectrum diagram for the lower stable state, (**c**) the spectrum diagram for the upper stable state.
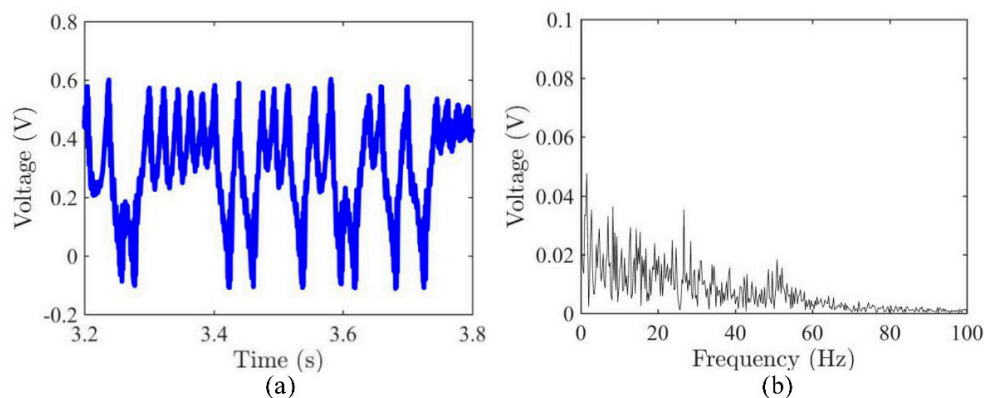
Figure 7. The dynamic snap-through for the voltage output, (**a**) the time-history graph, (**b**) the spectrum diagram.
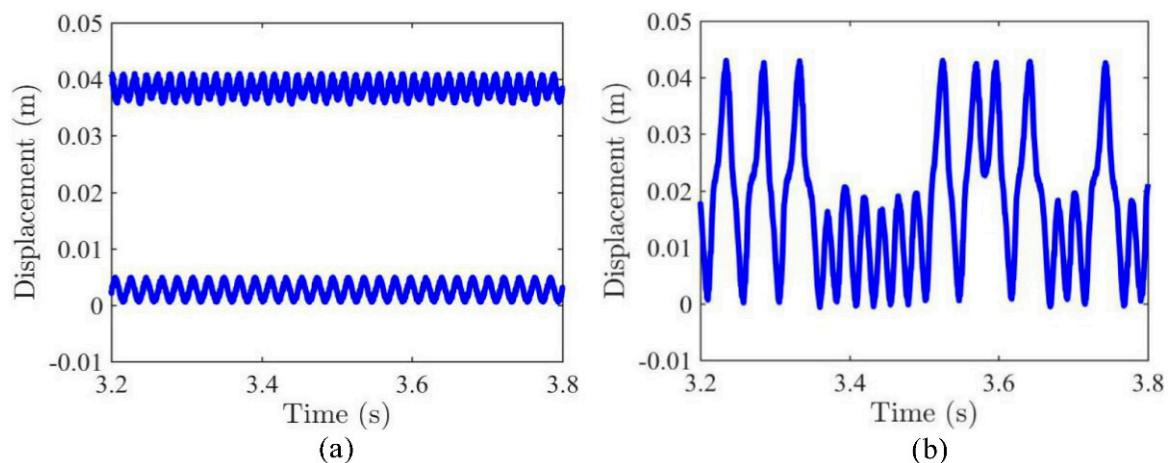
Figure 8. The vibrations of the asymmetric bistable composite laminated shell, (**a**) the vibrations around the two stable states respectively, (**b**) the dynamic snap-through between the two stable states.
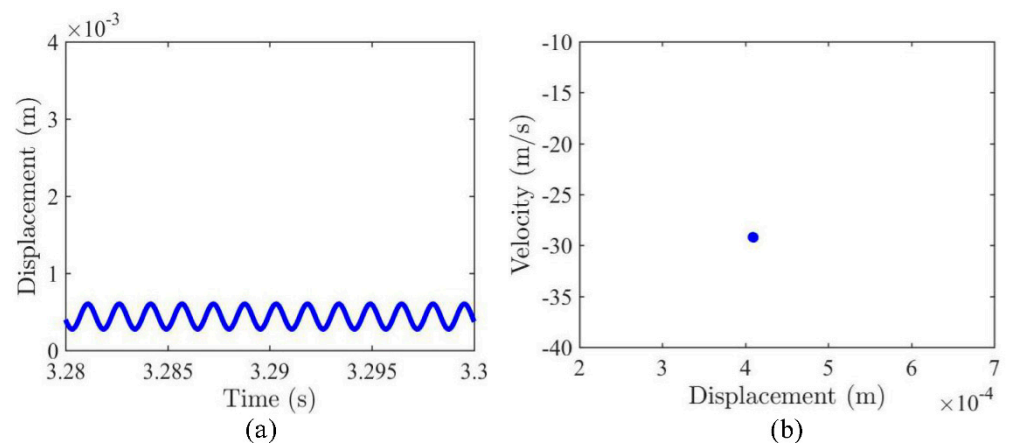
Figure 9. The periodic vibration, (**a**) the time-history graph, (**b**) the Poincaré map.
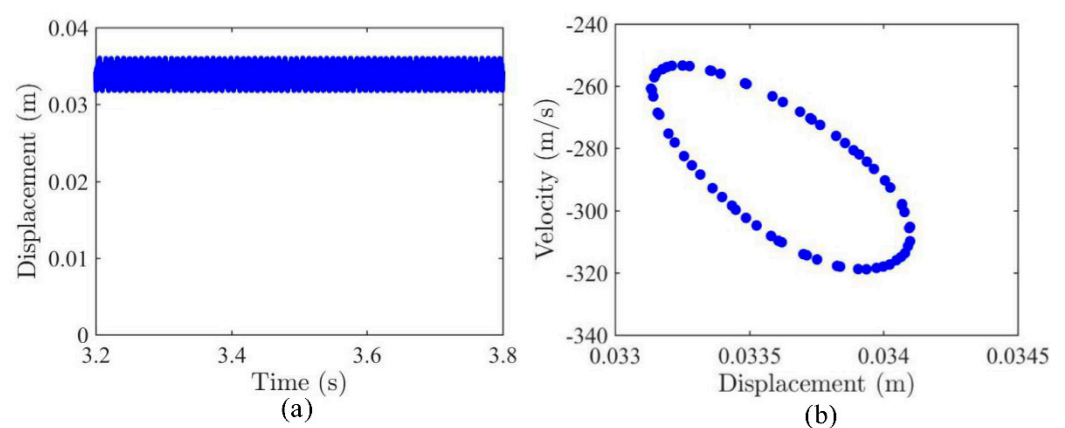
Figure 10. The quasi-periodic vibration, (**a**) the time-history graph, (**b**) the Poincaré map.

3.2. Frequency Sweeping

The Runge–Kutta method is adopted to solve the dimensionless Equations (53)–(55). Dimensionless symbols are omitted in Equations (53)–(55) for convenience. A series of bifurcation diagrams can be obtained shown in Figures 12–14 by sweeping frequency while keeping the amplitude constant. Figure 12 shows the bifurcation diagrams for displacement w and voltage output V by sweeping frequency when $f = 0.2$. Figure 13

shows the bifurcation diagrams for displacement w and voltage output V by sweeping frequency when $f = 0.3$. Figure 14 shows the bifurcation diagrams for displacement w and voltage output V by sweeping frequency when $f = 0.6$.
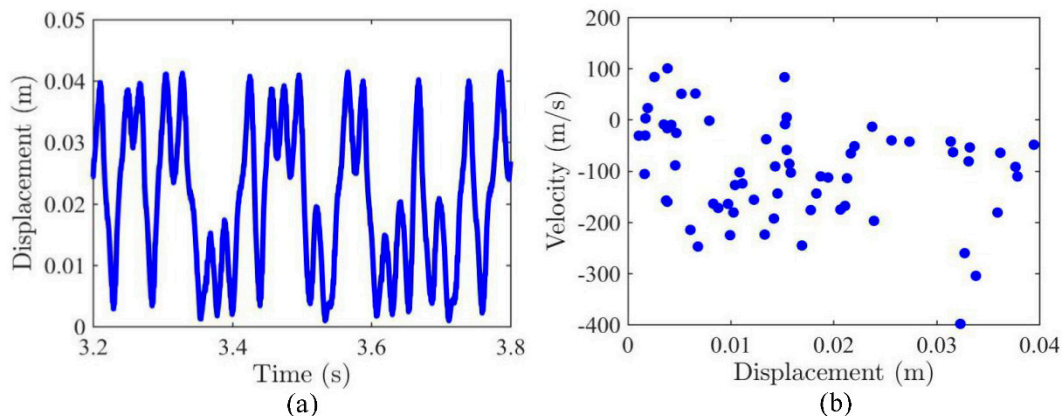
Figure 11. The dynamic snap-through and chaotic vibration, (**a**) the time-history graph, (**b**) the Poincaré map.
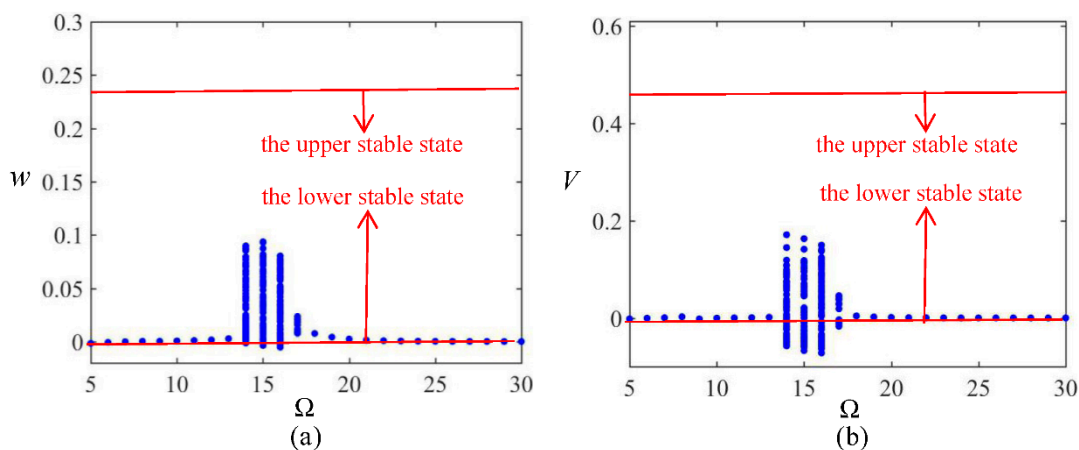
Figure 12. The bifurcation diagrams for displacement w and voltage V via the base excitation frequency Ω when amplitude $f = 0.2$, (**a**) the dynamic displacement, (**b**) the voltage output of harvester.
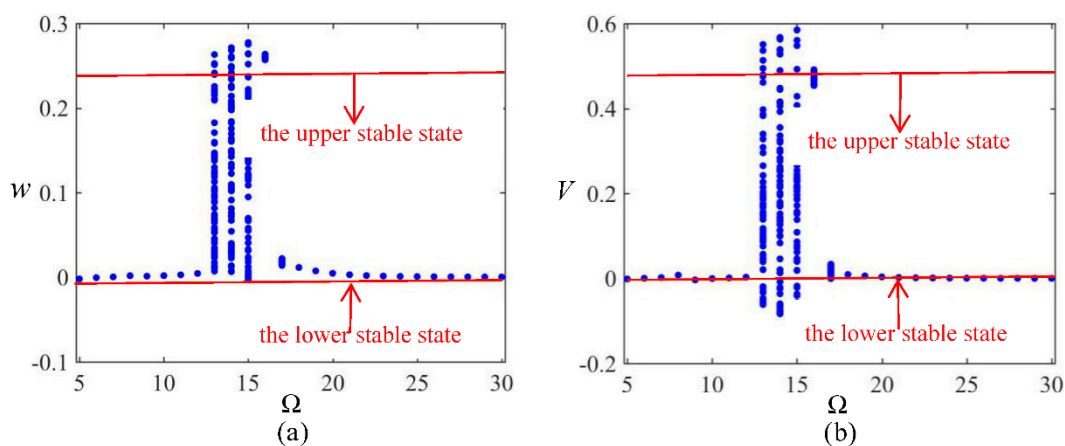
Figure 13. The bifurcation diagram for displacement w and voltage V via the base excitation frequency Ω when amplitude $f = 0.3$, (**a**) the dynamic displacement, (**b**) the voltage output of harvester.
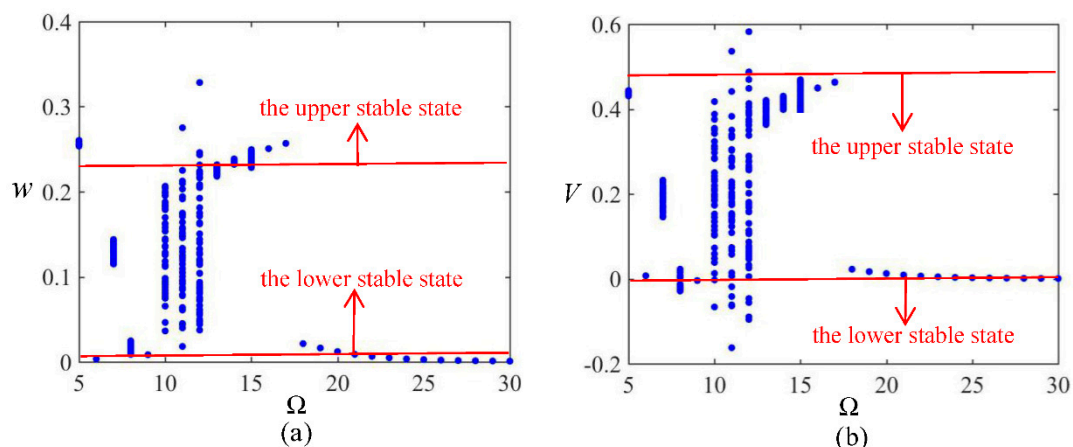
Figure 14. The bifurcation diagram for displacement w and voltage V via the base excitation frequency Ω when amplitude $f = 0.6$, (**a**) the dynamic displacement, (**b**) the voltage output of harvester.

The bistable energy harvester has two equilibrium positions shown in Figures 12–14 due to the two stable equilibrium states of the asymmetric bistable composite laminated shell. As shown in Figures 12–14, when the frequency for the base excitation with an appropriate amplitude is located in a particular range, the bistable system is found to vibrate between the two equilibrium positions, denoting the dynamic snap-through, while when the frequency is outside this particular range, the bistable system is found to vibrate around an equilibrium position.

Deploying an amplitude of 0.3, the frequency range for the base excitation, where the bistable system vibrates violently between the two equilibrium positions, denoting the dynamic snap-through, is 13~15 shown in Figure 13. Nevertheless, when the amplitude varies from 0.3 to 0.6, the frequency range where the dynamic snap-through can be found to occur migrates from 13~15 to 10~12 shown in Figure 14. The major reason why the frequency range migrates with the increase of the amplitude is the softening nonlinearity of the bistable system. The softening characteristics are detected based on the amplitude-frequency curve shown in Figure 15. The bistable system is a softening nonlinear system due to its negative stiffness. When the excitation amplitude increases gradually, the softening nonlinearity of the bistable system is enhanced during frequency sweeping, leading to the migration of the frequency range for the dynamic snap-through.
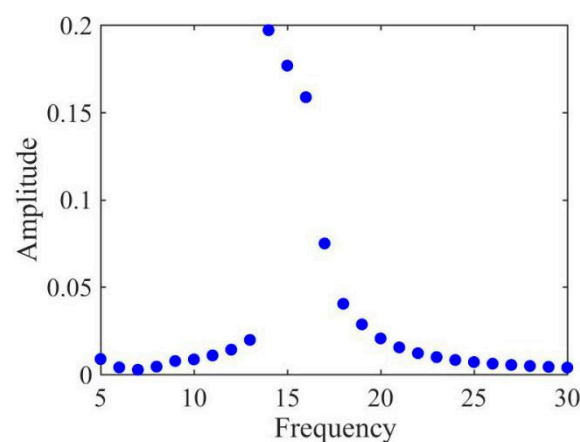
Figure 15. The amplitude-frequency curve for the voltage output.

The voltage output can also be elucidated in Figures 12–14. With an amplitude of 0.2, the small-amplitude voltage revolves round the upper equilibrium position during frequency sweeping shown in Figure 12, which is similar to that of conventional nonlinear

energy harvesters with a single potential well. At an amplitude of 0.3, the bistability is exhibited in the process of frequency sweeping. Due to the two equilibrium positions, the voltage output of the bistable energy harvester behaves as the large-amplitude dynamic snap-through and nonlinear vibrations with two potential wells shown in Figures 13 and 14. Comparing Figures 12 and 13, the amplitude of the latter voltage is three times that of the former voltage. Due to the large-amplitude dynamic snap-through and nonlinear vibrations with two potential wells, the bistable energy harvester produces large strains and in turn generates large power.

3.3. Amplitude Sweeping

Analogy to the previous section, the Runge–Kutta method is adopted to solve the dimensionless Equations (53)–(55) and dimensionless symbols are omitted in Equations (53)–(55) for convenience. A series of bifurcation diagrams can be obtained shown in Figures 16–20 by sweeping amplitude while keeping the frequency constant. When the amplitude for the base excitation with an appropriate frequency is located in a particular range shown in Figures 17–19, the bistable system is found to vibrate between the two equilibrium positions, denoting the dynamic snap-through, while when the amplitude is outside this particular range, the bistable system is found to vibrate around an equilibrium position. During amplitude sweeping with the too small excitation frequency shown in Figure 16 and the too large excitation frequency shown in Figure 20, the bistable system is found to vibrate around an equilibrium position.
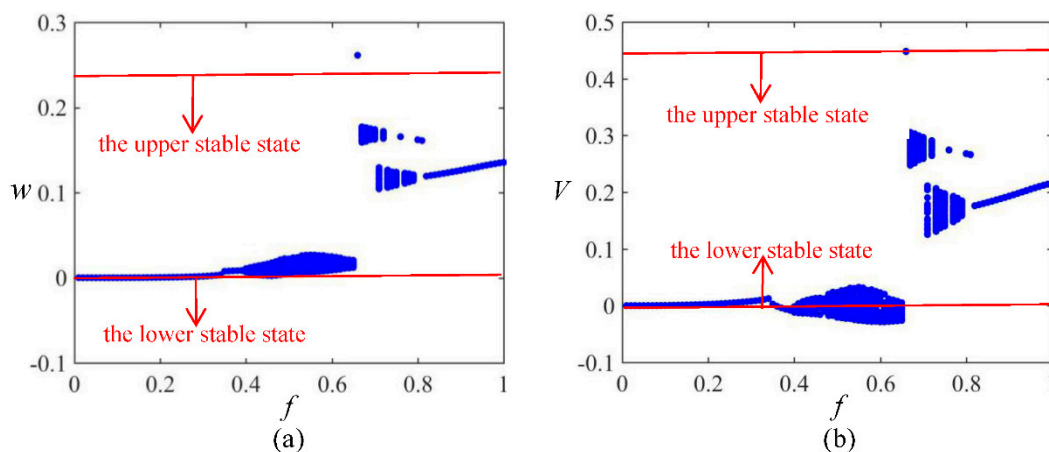
Figure 16. The bifurcation diagram for displacement w and voltage V via the base excitation amplitude f when frequency $\Omega = 8$, (**a**) the dynamic displacement, (**b**) the voltage output of harvester.
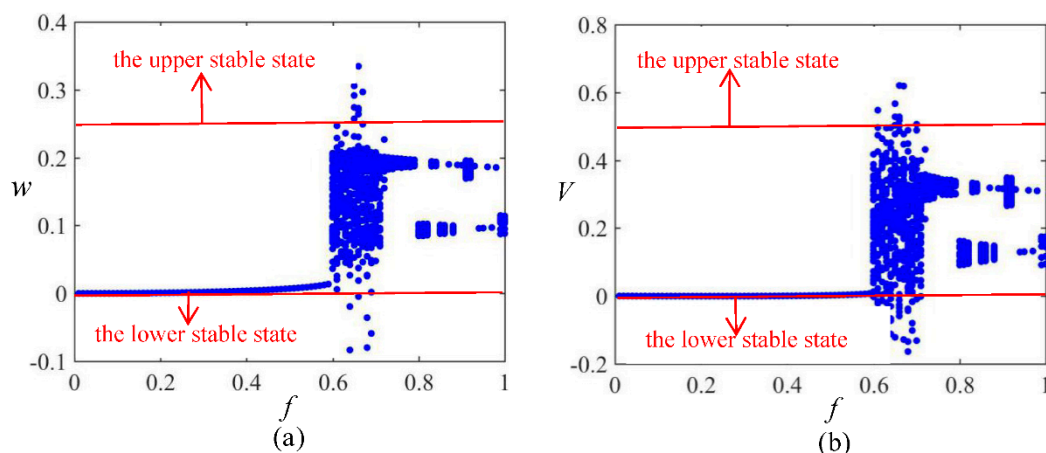
Figure 17. The bifurcation diagram for displacement w and voltage V via the base excitation amplitude f when frequency $\Omega = 10$, (**a**) the dynamic displacement, (**b**) the voltage output of harvester.
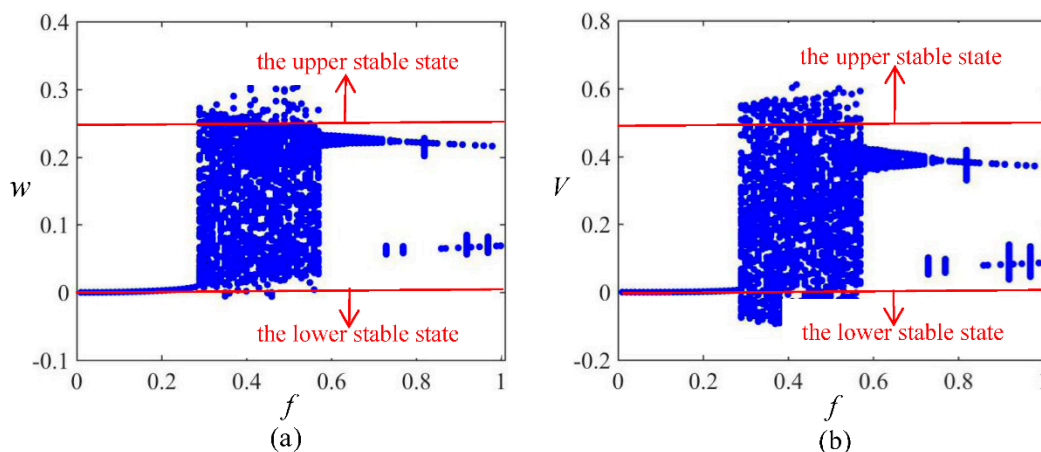
Figure 18. The bifurcation diagram for displacement w and voltage V via the base excitation amplitude f when frequency $\Omega = 13$, (**a**) the dynamic displacement, (**b**) the voltage output of harvester.
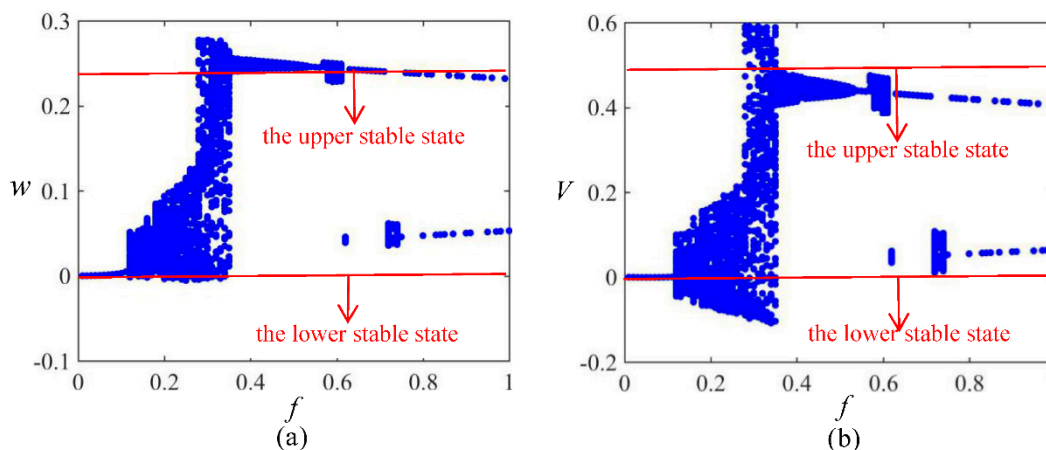
Figure 19. The bifurcation diagram for displacement w and voltage V via the base excitation amplitude f when frequency $\Omega = 15$, (**a**) the dynamic displacement, (**b**) the voltage output of harvester.
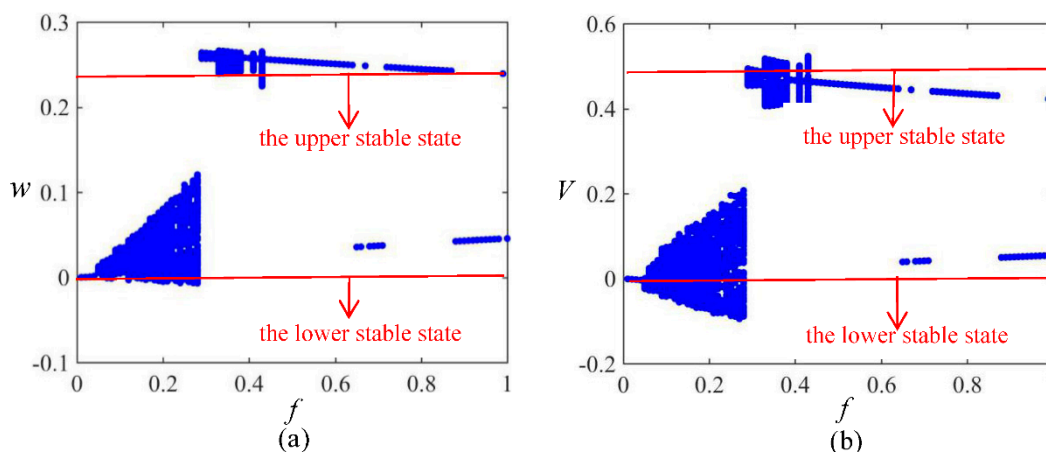
Figure 20. The bifurcation diagram for displacement w and voltage V via the base excitation amplitude f when frequency $\Omega = 16$, (**a**) the dynamic displacement, (**b**) the voltage output of harvester.

With a frequency of 8, the bistable system vibrates slightly around the lower equilibrium position during amplitude sweeping, which is similar to that of conventional nonlinear energy harvesters with a single potential well. With a slight increase in the fre-

quency, a very narrow amplitude range for the base excitation, where the large-amplitude dynamic snap-through and nonlinear vibrations with two potential wells can be induced, is identified. As the frequency continues to increase, the amplitude range for the base excitation where the dynamic snap-through can be found to occur widens first, then narrows, and finally disappears.

Deploying a frequency of 10, the amplitude range for the base excitation, where the bistable system vibrates violently between the two equilibrium positions, denoting the dynamic snap-through, is 0.6~0.7 shown in Figure 17. Nevertheless, when the frequency varies from 10 to 13, the amplitude range where the dynamic snap-through can be found to occur migrates from 0.6~0.7 to 0.3~0.6 shown in Figure 18. Continuing to increase the frequency to 15, the amplitude range for the base excitation migrates to 0.25~0.35. The major reason why the amplitude range migrates with the increase of the frequency is the softening nonlinearity of the bistable system. The bistable system is a softening nonlinear system due to its negative stiffness. When the excitation frequency increases gradually, the softening nonlinearity of the bistable system is enhanced during amplitude sweeping, leading to the migration of the amplitude range for the dynamic snap-through.

The voltage output can also be elucidated in Figures 16–20. With a frequency of 8, the small-amplitude voltage revolves round the upper equilibrium position during amplitude sweeping shown in Figure 16, which is similar to that of conventional nonlinear energy harvesters with a single potential well. At a frequency of 10, the bistability is exhibited in the process of amplitude sweeping shown in Figure 17. Due to the two equilibrium positions, the voltage output of the bistable energy harvester behaves as the large-amplitude dynamic snap-through and nonlinear vibrations with two potential wells shown in Figures 17–19. Comparing Figures 19 and 20, the amplitude of the former voltage is five times that of the latter voltage. Due to the large-amplitude dynamic snap-through and nonlinear vibrations with two potential wells, the bistable energy harvester produces large strains and in turn generates large power.

4. Conclusions

In this paper, the theoretical model on the dynamics of the energy harvester based on the asymmetric bistable composite laminated shell is established. The influence of the amplitude and the frequency for the base excitation on the bistable energy harvester is studied. The frequency sweeping with a constant amplitude and the amplitude sweeping with a constant frequency are carried out respectively.

When the frequency for the base excitation with a suitable amplitude is located in a specific range in the frequency sweeping or the amplitude for the base excitation with a suitable frequency is located in a specific range in the amplitude sweeping, the large-amplitude dynamic snap-through, nonlinear vibrations and voltage output with two potential wells can be found to occur. The amplitude and the frequency for the base excitation interact on each other for the specific frequency or amplitude range, that is to say, for the base excitation with different constant amplitudes in the frequency sweeping, the specific frequency ranges are different while for the base excitation with different constant frequencies in the amplitude sweeping, the specific frequency ranges are different.

The specific frequency or amplitude range for the base excitation, where the large-amplitude dynamic snap-through, nonlinear vibrations and voltage output with two potential wells can be found to occur, migrates due to the softening nonlinearity. The vibration in the process of the dynamic snap-through of the bistable system behaves as the chaotic vibration. The nonlinear vibrations of the bistable system behave as the periodic vibration, the quasi-periodic vibration and the chaotic vibration.

References

1. Emam, S.A.; Nayfeh, A.H. On the nonlinear bynamics of a buckled beam subjected to a primary-resonance excitation. *Nonlinear Dyn.* **2004**, *35*, 1–17. [CrossRef]
2. Abou-Rayan, A.M.; Nayfeh, A.H.; Mook, D.T. Nonlinear response of a parametrically excited buckled beam. *Nonlinear Dyn.* **1993**, *4*, 499–525. [CrossRef]
3. Lacarbonara, W.; Nayfeh, A.H.; Kreider, W. Experimental validation of reduction methods for nonlinear vibrations of distributed-parameter systems: Analysis of a buckled beam. *Nonlinear Dyn.* **1998**, *17*, 95–117. [CrossRef]
4. Daynes, S.; Potter, K.D.; Weaver, P.M. Bistable Prestressed Buckled Laminates. *Compos. Sci. Technol.* **2008**, *68*, 3431–3437. [CrossRef]
5. Li, H.; Dai, F.; Weaver, P.M.; Du, S. Bistable hybrid symmetric laminates. *Compos. Struct.* **2014**, *116*, 782–792. [CrossRef]
6. Daynes, S.; Nall, S.J.; Weaver, P.M.; Potter, K.D.; Margaris, P.; Mellor, P.H. Bistable composite flap for an airfoil. *J. Aircr.* **2010**, *47*, 334–338. [CrossRef]
7. Daynes, S.; Weaver, P.M.; Trevarthen, J.A. A morphing composite air inlet with multiple stable shape. *J. Intell. Mater. Syst. Struct.* **2011**, *22*, 961–973. [CrossRef]
8. Guest, S.D.; Pellegrino, S. Analytical models for bistable cylindrical shells. *Proc. R. Soc. A* **2006**, *462*, 839–854. [CrossRef]
9. Seffen, K.A. 'Morphing' bistable orthotropic elliptical shallow shells. *Proc. R. Soc. A* **2007**, *463*, 67–83. [CrossRef]
10. Brinkmeyer, A.; Santer, M.; Pirrera, A.; Weaver, P.M. Pseudo bistable self-actuated domes for morphing applications. *Int. J. Solids Struct.* **2012**, *49*, 1077–1087. [CrossRef]
11. Brinkmeyer, A.; Pirrera, A.; Santer, M.; Weaver, P.M. Pseudo bistable pre-stressed morphing composite panels. *Int. J. Solids Struct.* **2013**, *50*, 1033–1043. [CrossRef]
12. Coburn, B.H.; Pirrera, A.; Weaver, P.M.; Vidoli, S. Tristability of an orthotropic doubly curved shell. *Compos. Struct.* **2013**, *96*, 446–454. [CrossRef]
13. Eckstein, E.; Pirrera, A.; Weaver, P.M. Multi-mode morphing using initially curved composite plates. *Compos. Struct.* **2014**, *109*, 240–245. [CrossRef]
14. Hyer, M.W. Some observations on the cured shape of thin unsymmetric laminates. *J. Compos. Mater.* **1981**, *15*, 175–194. [CrossRef]
15. Hyer, M.W. Calculations of the room-temperature shapes of unsymmetric laminates. *J. Compos. Mater.* **1981**, *15*, 296–310. [CrossRef]
16. Hyer, M.W. The room-temperature shapes of four-layer unsymmetric cross-ply laminates. *J. Compos. Mater.* **1982**, *16*, 318–340. [CrossRef]
17. Peeters, L.J.B.; Powell, P.C.; Warnet, L. Thermally induced shapes of unsymmetric laminates. *J. Compos. Mater.* **1996**, *30*, 603–626. [CrossRef]
18. Schlecht, M.; Schulte, K.; Hyer, M.W. Advanced calculation of the room-temperature shapes of thin unsymmetric composite laminates. *Compos. Struct.* **1995**, *32*, 627–633. [CrossRef]

19. Schlecht, M.; Schulte, K. Advanced calculations of the room-temperature shapes of unsymmetric laminates. *J. Compos. Mater.* **1999**, *33*, 1472–1490. [CrossRef]
20. Cho, M.; Choi, M.H.; Chung, H.C.; Ahn, K.J.; Eom, Y.S. A study on the room-temperature curvature shapes of unsymmetric laminates including slippage effects. *J. Compos. Mater.* **1998**, *32*, 460–482. [CrossRef]
21. Gigliotti, M.; Wisnom, M.R.; Potter, K.D. Development of curvature during the cure of AS4/8552 [0/90] unsymmetric composite plates. *Compos. Sci. Technol.* **2003**, *63*, 187–197. [CrossRef]
22. Dai, F.; Li, H.; Du, S. Design and analysis of a tri-stable structure based on bi-stable laminates. *Compos. Part A* **2012**, *43*, 1497–1504. [CrossRef]
23. Dai, F.; Li, H.; Du, S. A multi-stable wavy skin based on bi-Stable laminates. *Compos. Part A* **2013**, *45*, 102–108. [CrossRef]
24. Dai, F.; Li, H.; Du, S. A multi-stable lattice structure and its snapthrough behavior Among Multiple States. *Compos. Struct.* **2013**, *97*, 56–63. [CrossRef]
25. Wang, G.Q.; Liao, W.H. A bistable piezoelectric oscillator with an elastic magnifier for energy harvesting enhancement. *J. Intell. Mater. Syst. Struct.* **2016**, *28*, 392–407. [CrossRef]
26. Cottone, F.; Basset, P.; Vocca, H.; Gammaitoni, L.; Bourouina, T. Bistable electromagnetic generator based on buckled beams for vibration energy harvesting. *J. Intell. Mater. Syst. Struct.* **2013**, *25*, 1484–1495. [CrossRef]
27. Harne, R.L.; Wang, K.W. A review of the recent research on vibration energy harvesting via bistable systems. *Smart Mater. Struct.* **2013**, *22*, 023001. [CrossRef]
28. Stanton, S.C.; Mcgehee, C.C.; Mann, B.P. Nonlinear dynamics for broadband energy harvesting: Investigation of a bistable piezoelectric inertial generator. *Phys. D Nonlinear Phenom.* **2010**, *239*, 640–653. [CrossRef]
29. Mann, B.P.; Owens, B.A. Investigations of a nonlinear energy harvester with a bistable potential well. *J. Sound Vib.* **2010**, *329*, 1215–1226. [CrossRef]
30. Arrieta, A.F.; Hagedorn, R.; Erturk, R.; Inman, R.J. A piezoelectric bistable plate for nonlinear broadband energy harvesting. *Appl. Phys. Lett.* **2010**, *97*, 174103. [CrossRef]
31. Lee, A.J.; Inman, D.J. A multifunctional bistable laminate: Snap-through morphing enabled by broadband energy harvesting. *J. Intell. Mater. Syst. Struct.* **2018**, *29*, 2528–2543. [CrossRef]
32. Syta, A.; Bowen, C.R.; Kim, H.A.; Rysak, A.; Litak, G. Experimental analysis of the dynamical response of energy harvesting devices based on bistable laminated plates. *Meccanica* **2015**, *50*, 1961–1970. [CrossRef]
33. Emam, S.A.; Hobeck, J.; Inman, D.J. Experimental investigation into the nonlinear dynamics of a bistable laminate. *Nonlinear Dyn.* **2019**, *95*, 3019–3039. [CrossRef]
34. Emam, S.A.; Inman, D.J. A review on bistable composite laminates for morphing and energy harvesting. *Appl. Mech. Rev.* **2015**, *67*, 060803. [CrossRef]
35. Pellegrini, S.P.; Tolou, N.; Schenk, M.; Herder, J.L. Bistable vibration energy harvesters: A review. *J. Intell. Mater. Syst. Struct.* **2013**, *24*, 1303–1312. [CrossRef]
36. Lu, Z.Q.; Shao, D.; Fang, Z.W.; Ding, H.; Chen, L.Q. Integrated vibration isolation and energy harvesting via a bistable piezo-composite plate. *J. Vib. Control* **2020**, *26*, 779–789. [CrossRef]
37. Borowiec, M.; Rysak, A.; Betts, D.N.; Bowen, C.R.; Kim, H.A.; Litak, G. Complex response of a bistable laminated plate: Multiscale entropy analysis. *Eur. Phys. J. Plus* **2014**, *129*, 1–7. [CrossRef]
38. Reddy, A.N. *Mechanics of Laminated Composite Plates and Shells: Theory and Analysis*; CRC Press: Boca Raton, FL, USA, 2004; pp. 200–216.
39. Pirrera, A.; Avitabile, D.; Weaver, P.M. Bistable plates for morphing structures: A refined analytical approach with high-order polynomials. *Int. J. Solids Struct.* **2010**, *47*, 3412–3425. [CrossRef]
40. Sembiring, L.; van Ormondt, M.; van Dongeren, A.; Roelvink, D. A validation of an operational wave and surge prediction system for the Dutch coast. *Nat. Hazards Earth Syst. Sci.* **2015**, *15*, 1231–1242. [CrossRef]
41. Gude, M.; Hufenbach, W.; Kirvel, C. Piezoelectrically driven morphing structures based on bistable unsymmetric laminates. *Compos. Struct.* **2011**, *93*, 377–382. [CrossRef]